Robust Local Thickness Estimation of Sub-Micrometer Specimen by 4D-STEM

Radim Skoupý, Daan B. Boltje, Miroslav Slouf, Kateřina Mrázová, Tomáš Láznička, Clémence M. Taisne, Vladislav Krzyžánek,* Jacob P. Hoogenboom,* and Arjen J. Jakobi*

A quantitative four-dimensional scanning transmission electron microscopy (4D-STEM) imaging technique (q4STEM) for local thickness estimation across amorphous specimen such as obtained by focused ion beam (FIB)-milling of lamellae for (cryo-)TEM analysis is presented. This study is based on measuring spatially resolved diffraction patterns to obtain the angular distribution of electron scattering, or the ratio of integrated virtual dark and bright field STEM signals, and their quantitative evaluation using Monte Carlo simulations. The method is independent of signal intensity calibrations and only requires knowledge of the detector geometry, which is invariant for a given instrument. This study demonstrates that the method yields robust thickness estimates for sub-micrometer amorphous specimen using both direct detection and light conversion 2D-STEM detectors in a coincident FIB-SEM and a conventional SEM. Due to its facile implementation and minimal dose reauirements, it is anticipated that this method will find applications for in situ thickness monitoring during lamella fabrication of beam-sensitive materials.

1. Introduction

Scanning transmission electron microscopy (STEM) is a powerful tool for studying thin specimens at high spatial resolution. In conventional 2D STEM modes, such as bright-field (BF), annular bright-field (ABF), annular dark-field (ADF) and high angle annular dark-field (HAADF), images are formed by integrating the total signal over a range of scattering angles in the diffraction plane as the focused STEM probe is scanned over a 2D area of a specimen. Geometrical sample properties along the image plane can be measured directly from the projection images. Obtaining information about properties along the beam direction is less straightforward. Yet, the ability to obtain 3D information can be highly relevant, for example, to accurately determine the sample thickness. A prominent example of the latter is in focused ion beam milling (FIB) of thin, large area lamellae for high-resolution imaging with TEM, where an optimized thickness may be needed to maximize recoverable information and obtain the highest resolution.[1–7] Determination of sample thickness during the milling process might thus allow the milling process to be stopped at precisely the required end-point and thereby improve both quality and throughput of sample preparation.

In SEM and TEM instruments, information along the z dimension of electron transparent samples can be obtained by backscattered electron imaging,[8] energy dispersive X-ray spectroscopy (EDX) analysis,[8,9] TEM tomography,[10] zero-loss TEM

R. Skoupý, K. Mrázová, T. Láznička, V. Krzyžánek
Institute of Scientific Instruments
Czech Academy of Sciences
Brno 61264, CZ
E-mail: krzyzanek@isibrno.cz
R. Skoupý, C. M. Taisne, A. J. Jakobi
Department of Bionanoscience
Delft University of Technology
Delft 2628 CD, NL
E-mail: a.jakobi@tudelft.nl

R. Skoupý
Kavli Institute of Nanoscience
Delft University of Technology
Delft 2628 CJ, NL
R. Skoupý, D. B. Boltje, J. P. Hoogenboom
Department of Imaging Physics
Delft University of Technology
Delft 2628 CJ, NL
E-mail: j.p.hoogenboom@tudelft.nl
M. Slouf
Institute of Macromolecular Chemistry
Czech Academy of Sciences
Prague 162 00, CZ

**ADVANCED
SCIENCE NEWS**

www.advancedsciencenews.com

**small
methods**

www.small-methods.com

imaging,[11] the calibration of secondary electron signal intensity ratio in the SEM image to electron energy loss spectroscopy (EELS) measurements,[12] or by comparison of a calibrated STEM image with a simulation of a known sample geometry, which is called quantitative STEM (qSTEM).[13,14]

Most methods require independent calibration before each imaging session to account for specific imaging settings. An additional disadvantage is that these methods may be difficult to implement in a FIB-SEM to allow for repeated in situ measurements during sample milling. Very basic calibrations link the image intensities to known sample characteristics originating from other imaging modalities, such as lamella thickness estimation using secondary electrons with STEM/EELS calibration.[12] Thickness-dependent changes in backscattered electron (BSE) signal intensity can also be calibrated via the signal of a standard sample of defined material/thickness,[8,15–17] or by using the differential detector response to a blanked electron beam (lower limit) and standard sample (upper limit).[18,19] The latter approach is often used for calibration of retractable BSE detectors because the geometry of this detector precludes exposure to the primary electron beam. For STEM detectors with suitable geometry, the detector response to the primary beam can be used for both calibration limits if fluence is chosen such that signal intensity remains within the dynamic range of the detector. This calibration method has been used in most qSTEM studies.[13,14,18,20] For BSE detectors, a reflection of the primary beam on an electron mirror can be used to reverse the direction of the primary beam toward the BSE detector.[21]

Intensity-based calibration methods have several practical disadvantages. First, the results are dependent on the time-dependent beam current or detector contrast/brightness settings, and hence different for each instrument and imaging condition. Second, calibration images may cover only a small part of the detector area (e.g., HAADF STEM segment) as its response may vary across the detector. Last, rotationally symmetric detectors have to be aligned to the electron optical axis to avoid systematic errors.

In contrast to regular STEM using segmented annular detectors, 4D STEM involves acquiring a 2D convergent beam electron diffraction pattern at every (x,y) pixel of a 2D STEM raster, yielding a 4D dataset with a spatially resolved diffraction pattern for each position across the specimen. 4D-STEM data analysis offers a broad range of methods to extract relevant information about the specimen from these spatially resolved scattering or diffraction patterns.[22–24]

Here, we present a local thickness estimation method that can be easily and repeatedly used not only for post acquisition data analysis but also during sample thinning by FIB milling. Our method uses the principles of quantitative 4D STEM (q4STEM) with a 2D STEM detector.[25,26] The method is free of signal intensity calibrations and provides accurate results in a wide thickness range from very thin (<50 nm) lamellae up to rough ones of about one micron thickness. Moreover, the applied electron dose can be reduced to a minimal level to mitigate primary beam sample damage.

2. Experimental Section

2.1. Demonstration Samples

2.1.1. Stepped Lamella

An epoxy resin block (hard type; $H_{111}C_{115}O_{24}$, $\rho = 1.245 \pm 0.013$ g cm^{-3}) was prepared as a test sample for lamella thickness estimation. The epoxy resin block was prepared according to manufacturer instructions by mixing epoxy embedding medium (Epon 812 substitute; 20 ml) with the hardeners methylnadic anhydride (MNA; 12 ml) and Dodecenylsuccinic anhydride (DDSA; 9 ml), and the accelerator 2,4,6-Tris(dimethylaminomethyl)phenol (DMP 30; 0.7 ml; Epoxy Embedding Medium kit, Sigma–Aldrich). The resin was poured into silicone moulds and cured at 60°C for 42 h. The density of cured resin blocks was determined pycnometricly. The cured block was then mounted on a aluminium sample stub using double-sided carbon tape. The stepped lamella was prepared by gallium milling on a Helios G4 HP FIB-SEM with a step height of 100 nm and step width of 600 nm. The steps range over a thickness from 100 nm up to 1200 nm. The final polishing was done at 30 keV beam energy with 18 pA probe current.

2.1.2. Latex Nanospheres

Polystyrene latex nanospheres (Agar SCIENTIFIC; $[C_8H_8]_n$, $\rho = 1.05$ g cm^{-3}) of three different diameters (S130-1: d=95 nm; S130-5: d=303 nm; S130-6 d=616 nm) were spread over thin continuous carbon ($\approx$5 nm)-covered gold TEM grid with 400 mesh density (Quantifoil Micro Tools).

2.1.3. Tissue Sections

Lung tissue (from female ICR mice) after continuous 12-week exposure in an inhalation chamber containing TiO_2 nanoparticles was embedded in an epon-durcupan mixture and cut to 100 nm sections.

2.2. Microscopes and Detectors

2.2.1. Direct Detection 2D-STEM Detector

The direct detection 2D-STEM experiments were performed on a Helios G4 HP FIB-SEM (Thermo Fisher Scientific; located at ISI Brno) equipped with a T-pix pixel array detector. The T-pix detector was composed of 256 × 256 pixels with a physical pixel size of 55 μm. The total active area of the detector is 14 × 14 mm and the detector was mounted at a detector-pole piece distance of 40 mm. The pixel saturation limit is 11,810 counts per pixel. In addition, the microscope was equipped with an annular STEM3+ detector (Thermo Fisher Scientific). All samples were imaged in field-free mode. The in-chamber configuration is shown in **Figure 1c**.
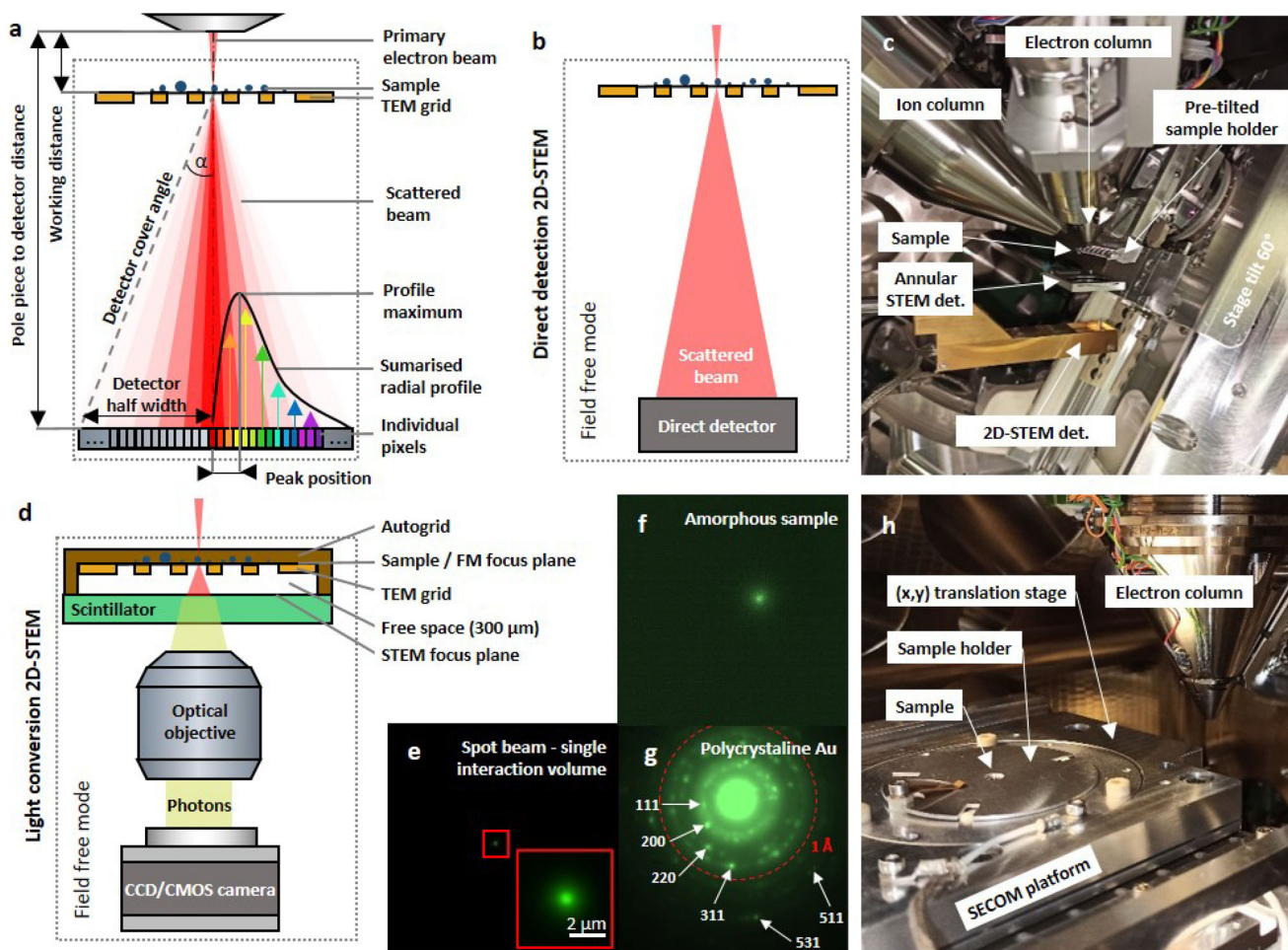
Figure 1. a) Principle of a geometrically calibrated quantitative STEM measurement using a 2D-STEM detector. The amount of electrons captured by individual pixels is azimuthally integrated according to their position on the detector. The distribution of the integrated signal carries information about the local thickness. **Direct detection 2D-STEM**: b) Schematic of the sample/detector geometry in direct detection 2D-STEM. The calibration distance from the sample to the detector is usually in the order of centimeters. c) In-chamber situation during annular STEM images acquisition. For 2D-STEM data acquisition the annular STEM detector has to be retracted. **Light conversion 2D-STEM**: d) Schematic of the sample/detector geometry for light-conversion 2D-STEM. The calibration distance from the sample to the scintillator in this case is given by the depth of TFS Autogrid (300 μm). e) 2D-STEM image of the single electron beam interaction volume (e-beam in spot mode). f) Transmission scattering pattern of a semi-thick amorphous sample (latex; ≈300 nm). g) Transmission diffraction pattern of gold nano-clusters (cropped and contrast-adjusted). h) In-chamber situation with the SECOM detector. The stage is not in the working position and will be moved under the electron column in operating mode. The optical objective is located below the sample holder on a separate xyz translation stage.

2.2.2. Light Conversion 2D-STEM Detector

The light conversion 2D-STEM experiments were done on a SEM Verios 460 (FEI - Thermo Fisher Scientific; located at TU Delft) equipped with a coincident fluorescence microscope SECOM (Delmic B.V.) equipped with a Zyla 4.2 PLUS sCMOS camera (Andor - Oxford Instruments). The original glass beam stopper was replaced with a YAG:Ce scintillator (thickness 0.15 mm, optical thickness for correction collar 0.18 mm). A Nikon S Plan Fluor 60 × /0.7 objective was used for its long working distance (2.6 – 1.8 mm).

2.2.3. Requirements for FIB/SEM Compatibility

For direct detection q4STEM, a pixelated 2D-STEM detector needs to be positioned underneath the sample. Usually, there is no conflict with regular sample stages, or they could readily be solved by the manufacturer of a FIB/SEM system. In our case, the stage had to be tilted to 60° and moved to y +45 mm to make space for insertion of the T-pix detector. The only resulting requirement was the need for a special pre-tilted sample holder. The whole setup is shown in detail in ref [27].

Table 1. Data acquisition settings for individual experiments.

Detector type	direct 2D-STEM		light 2D-STEM	
Sample	stepped lamella	lung section	latex beads	lung section
Image resolution	256 × 256	256 × 256	1024 × 1024	512 × 512
Beam energy [keV]	30	30	30	30
Probe current [pA]	6.3	25	25	50
Dwell time [ms]	20	10	3	2
Working distance [mm]	4.9	3.5	6.1	6.4
Detector cover semiangle [mrad]	177	171	353	353
Real pixel size [µm]	55	55	6.5	6.5
Demagnified pixel size [nm]	–	–	108	108
Step [nm]	75	20	20	15
Matrix size	250 × 175[a]	200 × 200[a]	99 × 99[a]	199 × 199[a]
Single scattering pattern file size [MB]	0.128	0.128	1	0.29
Full data cube file size [GB]	5.6	5.1	9.8	11.2

[a] only parts are shown in the figures

For light conversion q4STEM, the scintillation screen and optical microscope (which has to be coverslip corrected) was required and needed to be integrated in a SEM. In our case, the Delmic SECOM detector was integrated in a specific SEM-compatible door which replace the original one. As the original stage was mounted on the door, there was no positioning conflict.

2.3. Data Processing

2.3.1. Data Acquisition Settings

Imaging was performed as individual point measurements using spot mode with discrete distances between individual beam positions. Beam shift was used to move the beam across the samples. Data acquisition parameters can be found in **Table 1**.

2.3.2. Electron Scattering Simulations

Monte Carlo simulations of electron scattering were calculated in MONCA2, an evolution of the original Monte Carlo simulation package MONCA[28] running under MATLAB. 500,000 electrons with an energy of 13, 15, or 30 keV were used in each simulation (a single simulation run takes approximately 20 min on a single core of Intel Core i7-10700 CPU @2.90GHz; the produced data structure required approximately 500 MB of disk space). The resulting MCSA (most common scattering angle) and DF/BF (dark field/bright field) ratio dependencies were fitted with polynomial fits. Monte Carlo simulation results and the Matlab script for data processing were provided in the data repository (https://doi.org/10.4121/21365268).

2.3.3. PXRD Simulation

Theroretical powder X-ray diffraction (PXRD) patterns of TiO_2 were computed with the program PowderCell[29] using the crystal structure of TiO_2 (anatase modification) deposited in the Crystallography Open Database.[30]

Table 2. STEMDIFF settings.

Detector type	direct 2D-STEM	light 2D-STEM
ups	4	2
datap	40000	9801
cen_type	maximum	maximum
ent_type	ent	ent
normp	25	25
psfmed	1	1
detcov	0.5	0.3
decit	100	1000
ent_fil	0.1	0.045
bcg_value_low	0.45	0.051
bcg_value_high	0.65	0.065
files used	166	117

2.3.4. STEMDIFF Settings

Powder diffraction data were analyzed in *STEMDIFF - powder electron diffraction in SEM* available on the MathWorks File Exchange repository.[31] To replicate our results, settings shown in **Table 2** should be used.

3. Results

3.1. Principle

The main idea behind our q4STEM method is that electrons passing through electron transparent samples are scattered to higher angles with increasing sample thickness (or mass density). Thus, measuring the extent of electron beam spreading by the transmitted scattering signal allows estimating the local thickness. We present two ways in which this spreading can be quantified: 1) describing the most common scattering angle (MCSA), and 2) the ratio of integral signals in a specific angular range (DF/BF - dark field/bright field). Both can be readily computed

**ADVANCED
SCIENCE NEWS**

www.advancedsciencenews.com

**small
methods**

www.small-methods.com

from an integral radial profile of intensities in the scattering pattern (Figure 1a). This calculation consists of i) beam centre detection in each scattering pattern, ii) computing the azimuthally integrated intensities across a one pixel radial width, and iii) determination of the peak position from the resulting radial profile (for MCSA) or the area under curve across a given range of scattering angles (for DF/BF ratio). The resulting descriptors can then be converted into local thickness estimates by comparison to Monte Carlo simulations of electron scattering. Unfortunately, the expected "doughnut" shape of a scattering pattern passing through a thick amorphous sample is not visible directly, because the higher amount of recorded electrons at higher scattering angles is distributed over more pixels (by a factor of $2\pi r$, where r is the distance from the center).

While we acquire experimental data (MCSA, DF/BF ratio) in pixel units, simulation results are in angular units. To convert pixel position to scattering angles, the position of the 2D-STEM detector relative to the sample has to be known. In the SEM, the detector distance is typically a well-defined, invariable parameter. The use of a pixelated STEM detector has the additional advantage that it does not require detector alignment to the optical axis. When a segmented annular STEM detector is in an off-axis position, the detection geometry does not match that assumed in the simulation, which leads to incorrect thickness estimation. In the case of a 2D-STEM detector, the beam center can be detected and detector displacement corrections can be applied for each scattering pattern.

3.2. Direct Detection 2D-STEM Detector

For direct detection with a pixelated STEM detector, the detection geometry is straightforward (Figure 1b). The detector-to-sample distance, and thus the accessible angular scattering range, can be slightly adjusted by a change in working distance as typically the detector is mounted at a fixed distance from the objective lens pole-piece.

Figure 1c shows the in-chamber view in the FIB-SEM. This configuration with a retractable annular STEM detector enables easier and faster navigation across the sample in combination with acquisition of 4D-STEM data, as virtual STEM images based on 4D-STEM data take significantly more time to acquire. The annular STEM detector images are used for region of interest (ROI) localization at high precision. Subsequently, 4D-STEM data cubes are taken at these positions. In our configuration, the original sample stage has to be tilted to 60° to make sufficient space for 2D-STEM detector.

3.3. Light Conversion 2D-STEM Detector

Implementation of our q4STEM method is not limited to direct detection 2D-STEM detectors. As an example of an alternative approach, we turned a retrofittable integrated light microscope (SECOM; DELMIC B.V.) into a high-resolution 2D-STEM detector, referred to as light conversion 2D-STEM (principle shown in Figure 1d). The main idea lies in replacing the original glass coverslip protecting the objective lens with an electron-sensitive scintillator (Figure 1d).

The idea of a scintillator screen together with the SECOM detector is not new. A similar solution is used in the optical STEM method[32] that is used for multibeam detection in the FAST-EM.[33] In optical STEM, the sample is placed directly on the scintillator. For q4STEM, a precisely determined free space is introduced between the sample (on a TEM grid) and the scintillator. We achieved this by clamping the TEM grid into an AutoGrid (Thermo Fisher Scientific), which has well-defined dimensions with an inner depth of $300^{+0}_{-20}\,\mu m$ (Figure 1d). The scintillator is then used as a screen by which the electron scattering patterns are converted to a light signal that can be visualized with the optical microscope.

The light-conversion 2D STEM detection setup allows switching imaging mode from light microscopy to 2D-STEM by changing the objective lens focus. The upper focus plane is at the level of the sample – enabling reflection and fluorescence imaging, while the lower focus plane is located a few microns under the upper scintillator surface – enabling 2D-STEM image acquisition. In this position an image of the interaction volume can be acquired (Figure 1e) and the scattering pattern of an amorphous sample (Figure 1f), or the diffraction pattern of polycrystalline samples (Figure 1g) can be recorded. Diffraction analysis using a fluorescent screen and light detecting camera has been reported previously[34] but in this case the viewing solid angle was significantly lower than that accessible in our system (3.83×10^{-3} sr compared to 1.54 sr). As a result, our method allows the use of several orders of magnitude lower beam currents, enabling application to beam sensitive samples. The in-chamber view on our setup is shown in Figure 1h.

3.4. Data Processing

In our q4STEM method, a scattering pattern is recorded for each beam position. In each scattering pattern, the beam center is detected first (**Figure 2**a, usually the pixel with the highest intensity) and the image is cropped to the area containing the scattering pattern (Figure 2b: smaller size, maximum in the middle). The preprocessed ROI image is then processed differently depending on whether the data comes from a light conversion 2D-STEM detector, where image background subtraction is needed (Figure 2c,d) or from direct detection 2D-STEM, where the radial profile can be calculated directly. Here, the experimental data are fitted with a polynomial function in order to smooth the noisy raw profiles and to detect the peak position, which we refer to as the most common scattering angle (MCSA) (Figure 2e). The DF/BF ratio can be calculated directly from the raw data by computing the integral signals in the low angular range (BF, 0–50 mrad) and intermediate angular range (DF, 50–100 mrad; Figure 2g). Note that these angular ranges are chosen such that they maintain nearly linear dependence in the required range of thicknesses. The descriptors (MCSA and DF/BF ratio) are then compared with results of Monte Carlo simulations of electron scattering with a known sample geometry (Figure 2f,h) yielding a sample thickness estimate for this beam position. By repeating this procedure for the scattering pattern recorded at each scan beam position, the sample thickness is calculated for each data point. As a result, the above procedure can run in parallel in order to reduce computing time and create position-dependent local thickness maps.
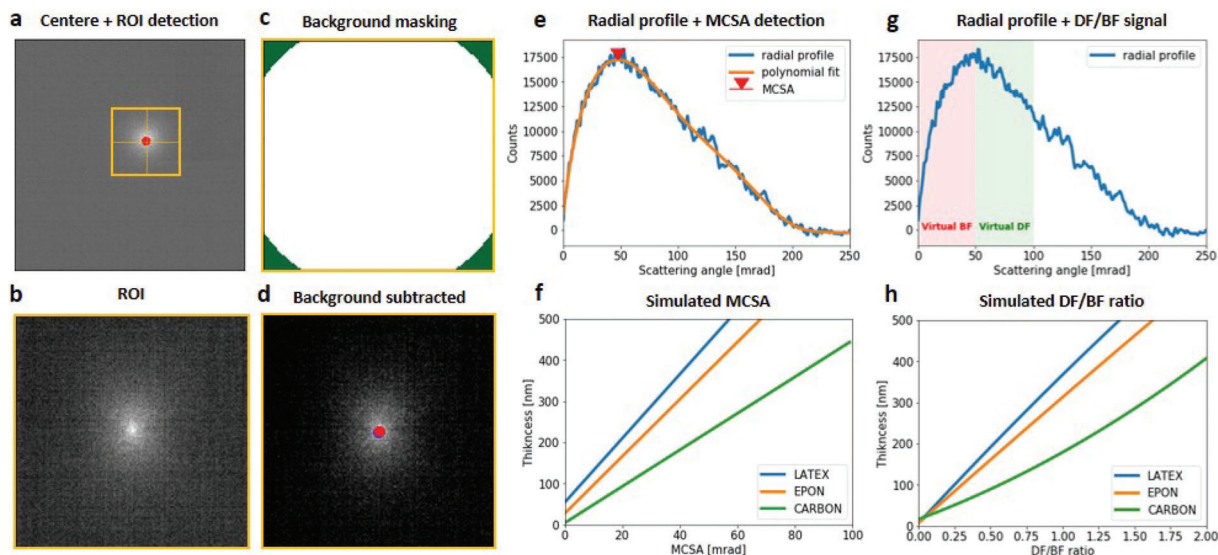
Figure 2. Data processing pipeline for local thickness measurements with q4STEM. a) In the full-scale image as obtained from the detector, the center of the scattering pattern is determined (in red) and a region of interest (ROI) is defined such as to cover the entire 100 mrad scattering angle. b) Data outside the ROI is removed and the cropped ROI is kept for further processing. c) For light conversion 2D-STEM, a circular mask is used for background subtraction, where the background level is taken as the mean pixel intensity of the corner areas (in green). d) ROI image after background subtraction. e) In the MCSA approach, the scattering pattern is azimuthally integrated and its peak position determined. The corresponding scattering angle is then compared to f) the result of Monte Carlo simulations giving the peak position versus sample thickness up to 500 nm. The comparison yields an estimated local sample thickness. g) In the DF/BF approach, the integral signals of virtual BF (0–50 mrad) and DF (50–100 mrad) segments are determined and the ratio of DF/BF signal intensity is then compared to h) the DF/BF ratios obtained from Monte Carlo simulations for a sample thickness up to 500 nm, again to yield a local sample thickness.

Due to the nature of the thickness descriptors (MCSA resp. DF/BF signal ratio) the results are independent of the absolute intensity values in the initial images. However, there are necessary prerequisites such as a linear detector response to the cumulative electron dose, and homogeneous detector sensitivity across all pixels. Besides, it is mandatory to avoid detector saturation, which can affect the shape of the radial profile. Another prerequisite for the MCSA q4STEM method is a well-defined peak in the radial profile. For very thin samples, no peak is observed, and the scattering profile is monotonically decreasing, as shown for a polymer nanosphere sample in **Figure 3**a. This limits the lower bound for the thickness estimation using the MCSA method (sample/material dependent; ≈100 nm for latex).

For both methods, the crucial point is the accurate detection of the center of the scattering pattern during the first processing step. The DF/BF ratio method shows higher robustness to center mismatch due to signal integration across relatively wide areas. A small error in the true center position is therefore negligible. On the contrary, the position of the MCSA directly depends on the shape of the radial profile, which is highly sensitive to the center position.

Both thickness estimation methods are based on the same primary data and can be calculated at once. The final results from both methods should be consistent, allowing detection of possible errors in data processing or data acquisition. For medium/high thickness (> 300 nm for nanospheres), the angular range for analysis has to be chosen larger than 100 mrad to avoid unwanted signal changes during background subtraction (a larger range limits the center dislocation correction).

3.5. Optimal Beam Energy

In addition to the residual error in the primary beam position, the accuracy of thickness estimation by our method depends critically on the primary beam energy, where lower energies result in increased signal modulation (MCSA or DF/BF ratio) with changing thickness. Thus, one may expect that low beam energies lead to higher accuracy in the case of thin samples. This, however, is not generally applicable with light conversion 2D-STEM as shown in Figure 3e, where the scattering pattern becomes blurred for thicker samples and lower beam energies, and affects accuracy of the center detection step during data processing. Errors in centre position may drastically affect the resulting accuracy of thickness estimation using the MCSA method. This effect is more pronounced for the light conversion 2D-STEM detector where background noise is higher compared to direct detection 2D-STEM (Figure 3e,f). Moreover, in order to limit beam damage induced by the transmitted electron beam, a higher beam energy is preferred because less energy is absorbed in the sample from inelastic scattering. For these reasons, we used the maximal SEM energy of 30 keV in all experiments.

3.6. Detector Resolution

To record radial profiles suitable for MCSA detection and retrieval, the angular distribution of scattered intensities needs to be sampled finely enough and cover a specific angular range. On a pixelated detector these are determined by the detector coverage angle and the angular increment covered by individual
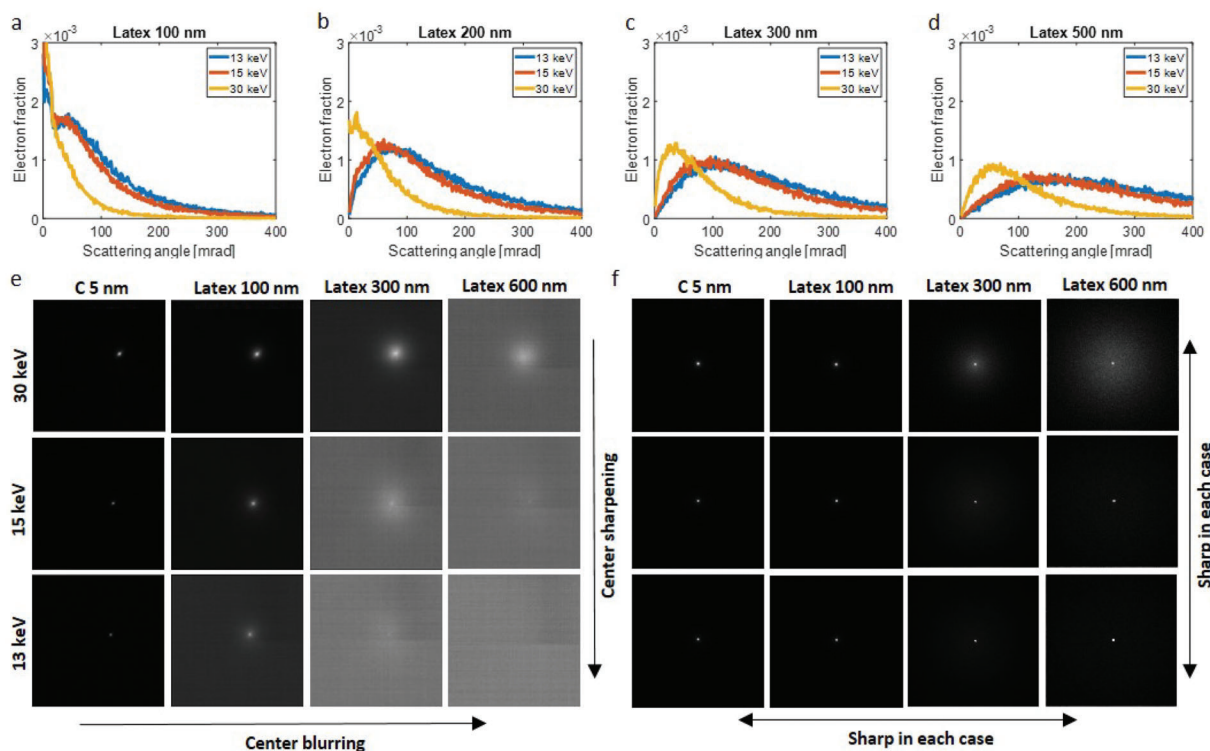
**ADVANCED
SCIENCE NEWS**

www.advancedsciencenews.com

**small
methods**

www.small-methods.com

Figure 3. Determination of optimal beam energy. Simulated angular distribution of scattered electrons: a) For a 100 nm polymer nanosphere sample, a sharp maximum in the radial profile needed for the MCSA method is only observed at 13 keV, while imaging with 15 keV yields a plateau with non-discernible peak position and for 30 keV electrons a monotonically decreasing profile is observed. Conversely, all three beam energies are suitable for thickness estimation by the DF/BF method. b-d) For 200–500 nm nanospheres, all three electron energies produce recognizable maxima in their angular distributions. Scattering pattern center detection: e) Scattering patterns acquired with a light conversion 2D-STEM detector show blurring with decreasing beam energy and increasing sample thickness. f) Scattering patterns acquired with a direct detection 2D-STEM detector show consistent profiles across all beam energies due to very low background.

pixels (that determines the angular sampling of the recorded radial profile). These parameters may be affected by sample-to-detector distance and, in the case of the light conversion detector, by objective magnification. From our experiments, we know that 0.7 mrad per pixel is sufficient for appropriate sampling (the T-pix detector has 0.678 mrad per pixel, while the SECOM with quadruple binning, resulting in 512×512 pixels, has 0.689 mrad per pixel). Coarser sampling would benefit from reduced electron exposure (as the signal per individual pixel is effectively increased) but would suffer from lower precision in thickness estimation due to the coarse sampling.

3.7. Proof of Concept

3.7.1. Direct Detection q4STEM

We applied geometric calibration of local thickness using a FIB-milled stepped lamella after lift-out from a bulk epoxy resin block. The geometric parameters of the stepped lamella were chosen in order to obtain a set of well-defined areas with known thickness. We prepared twelve steps with an individual height of 100 nm and a step width of 600 nm, thus creating a thickness range from 100 nm up to 1200 nm (**Figure 4**a). We then mapped an area of interest and estimated the local thickness (Figure 4b) by direct

detection of 2D-STEM as described above. The local thickness across the individual stripes was transversely averaged and plotted according to the lateral position of its long axis (Figure 4c). The cross-sections of linear fits with the border of the lamella give the thickness of the lamella at its edge. In the low thickness region (100–400 nm), the real edge was damaged during milling and thus these values are extrapolated.

The final accuracy as given by comparison of measured and geometrical thickness shows very small deviations, lower than 10 % relative or 25 nm absolute error across the entire thickness range except for the thinnest and thickest step (100 and 1200 nm respectively; Figure 4d). These values are also outside the measuring range of the MCSA method for this epoxy resin sample and using a 30 keV primary beam. Interestingly, the measured wedge angle is very similar for all stripes and varies around 2° – the lamella was generated without over-tilting as typically used for bi-planar shape creation.

3.7.2. Light Conversion q4STEM

To demonstrate thickness estimation with the light conversion 2D-STEM detector, we mapped a sample of latex nanospheres with varying diameters (Figure 4e). The chosen area contains numerous 95 nm, several 303 nm and two 616 nm beads (nominal
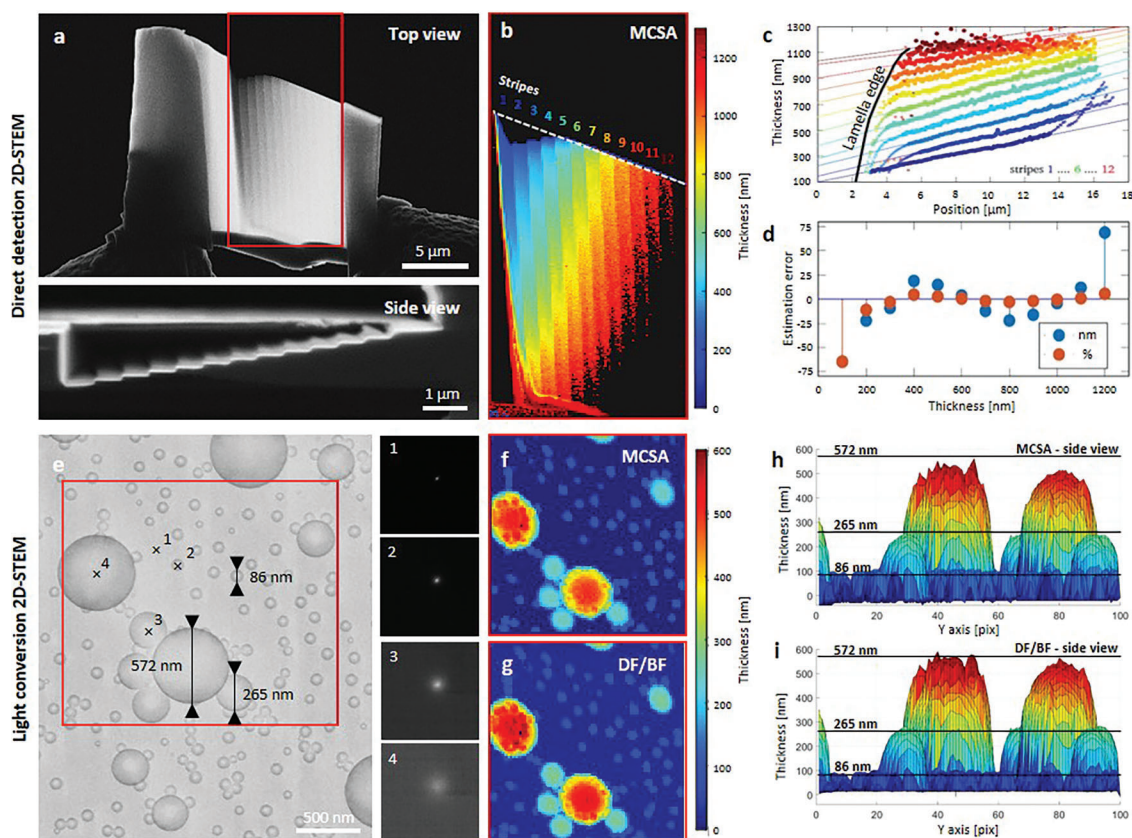
ADVANCED
SCIENCE NEWS
www.advancedsciencenews.com

small
methods
www.small-methods.com

Figure 4. Demonstration of local thickness measurement on FIB-milled stepped lamella and polymer nanospheres. Direct detection 2D-STEM: a) Stepped lamella prepared by FIB milling (BF STEM image on top, side-view secondary electron image on bottom). The mapped area is marked in red. b) Thickness map resulting from MCSA analysis. The original lamella edge is indicated by the white dashed line. c) Individual step thickness profiles. Symbol colours correspond to stripe numbers in (b), based on intended edge-thickness of each step. Solid lines indicate linear fits to the data for each stripe while the thick black line indicates the lamella edge (their intersections yield the lamella thickness on its original edge). d) Estimated errors in the determined thickness show high accuracy except for the thinnest and thickest stripes that exceed the MCSA method limits of 200 nm and 1100 nm for this sample. Light conversion 2D-STEM: e) Three-beads sample on a continuous carbon film, positions indicated with numbered cross marks highlight where the scattering patterns were recorded. f) Thickness map based on MCSA method. g) Thickness map based on DF/BF ratio method. h) Side-view of the MCSA map. i) Side-view of the DF/BF map. Note: results are corrected for the supporting carbon film; measured diameters of the beads are indicated by black lines (86, 265, and 572 nm respectively) and correspond well with the retrieved thickness profiles, especially for the DF/BF ratio method.

diameters). The thickness maps resulting from the individual thickness estimation methods (MCSA - projection in Figure 4f, profile in Figure 4h) and DF/BF ratio - projection in Figure 4g, profile in Figure 4i) differ in the accuracy achieved. Both methods match the real sample thickness in the case of small and middle beads (diameter = thickness in the center), but the MCSA map slightly underestimates the largest beads compared to the DF/BF map, which shows very good correspondence. The mismatch is possibly caused by imperfect center detection during data processing or excessive data trimming during cropping of the scattering pattern ROI. This could potentially be improved by extending the angular range beyond 100 mrad.

3.8. Combined Amorphous/Crystalline Sample Analysis

Our local thickness estimation method can be combined with other 4D-STEM techniques based on the same 4D data cube.

For both direct detection and light conversion 2D-STEM modalities, we demonstrate such an application on epoxy resin embedded mouse lung tissue containing inhaled TiO_2 particles in **Figure 5**. The same sample was analyzed using both detectors, where the areas of interest (a,e) were mapped and analyzed with both q4STEM and powder nanobeam diffraction analysis. Resulting thickness maps (Figure 5b,f) show variation between individual sections ($\approx$30 nm). We note that the thickness retrieved for the nanoparticles is not correct due to their atomic composition, density and crystallinity, which differ from the reference material (amorphous epoxy resin) to which the observed scattering patterns are compared to in this case. Specific information on, and identification of, these nanoparticles can be achieved with the recently-introduced 4D-STEM/PNBD method (powder nanobeam diffraction calculated from 4D-STEM data).[27,35] Ordinary SEM analytical techniques (such as STEM imaging and EDX analysis) could reveal the presence of TiO_2, but they could not confirm the crystalline modification of TiO_2

ADVANCED
SCIENCE NEWS

www.advancedsciencenews.com
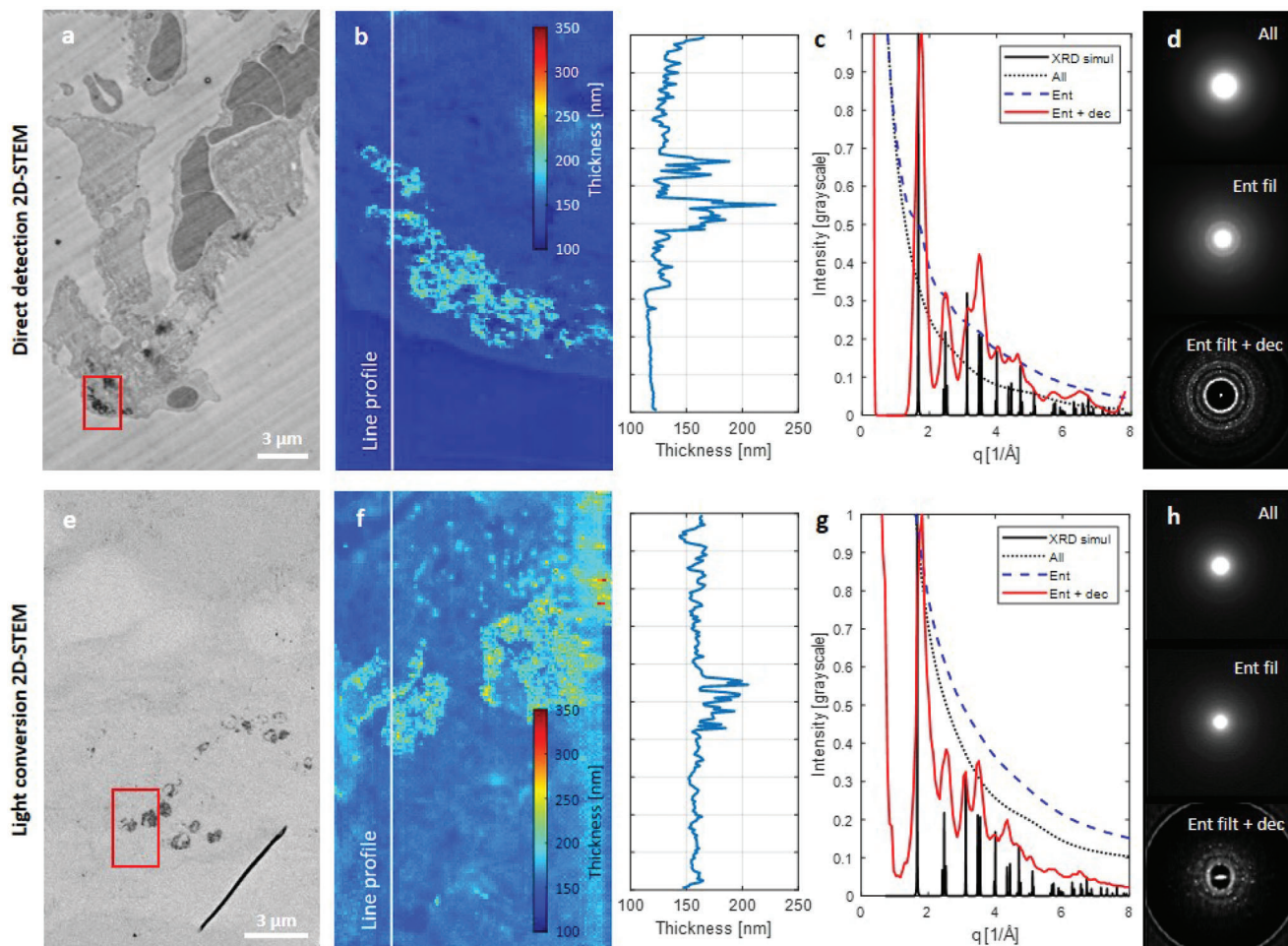
small
methods

www.small-methods.com

Figure 5. Combined analysis of an amorphous-crystalline sample from a single 4D-STEM data cube. Direct detection 2D-STEM in panels (a–d), Light conversion 2D-STEM in panels (e–h). a,e) Ultrathin section of mouse lung tissue after TiO_2 inhalation exposure. b,f) Thickness maps from the areas highlighted with red boxes in a,e. The line profiles were taken at the position of the solid white line. c,g) Radial profiles of resulting powder diffractograms. Deconvolution significantly enhances the profile of anatase. d,h) Powder diffractograms of *all* points, *entropy filtered* and *entropy filtered + deconvolution*, respectively.

nanoparticles. The new 4D-STEM/PNBD methods yields 2D powder electron diffractograms (Figure 5d,h) and their 1D radial profiles (Figure 5c,g). The comparison of experimental powder electron diffractograms with theoretically calculated powder X-ray diffraction patterns showed that the TiO_2 nanoparticles exhibited the anatase modification, which is unique additional information from the recorded 4D data cube.

4. Conclusion

We have demonstrated the principle and implementation of a robust geometrically calibrated method for lamella thickness estimation by 4D-STEM in a (FIB)-SEM. The combined DF/BF - MCSA method allows mapping local sample thickness at high accuracy in the range up to ≈1 µm and it can be used with any 2D-STEM detector type, as shown with both commercial direct detection 2D-STEM and light-converted 2D-STEM detectors. The lower limit for thickness estimation of the MCSA method is dependent on the presence of a discernible peak

in the angular electron scattering distribution. As our method measures mass-thickness, the upper limit is linearly dependent on the reciprocal sample density (≈1300 nm for latex, ≈1100 nm for epoxy resin, and ≈650 nm for amorphous carbon; all for 30 keV beam).

The main advantages of our q4STEM method are the stable and time-invariant calibration given by detection geometry, the simple result interpretation where higher MCSA and DF/BF ratio mean higher thickness, its applicability over a wide range of relevant sample thicknesses, and its robustness to beam tilt introduced during beam scanning. At 500× magnification (horizontal field width 829 µm), the introduced beam tilt of 17.9 mrad affects the estimated thickness by a factor of 0.016 %. At higher magnifications of 1000× and 5000× the estimated errors would be 34 and 1 ppm, respectively.

On the other hand the method requires a priori knowledge on the sample composition as input for simulations of electron scattering, and is limited to measuring only pure amorphous matrix material in heterogeneous samples, e.g., resin in case of

biological thin sections. The thickness of crystalline samples can be approximated only if they are contained within an amorphous matrix. In addition, particularly for light conversion 2D-STEM, the short sample to detector distance makes the method sensitive to small deviations such that, for example, large mechanical tolerances of the sample mount or grid curvature may lead to inaccuracies in the estimated thickness.

We see the main application for the q4STEM method in combination with FIB-SEM sample preparation for in situ lamella thickness control. While still to be demonstrated for cryogenic conditions and samples, q4STEM thickness estimation could be integrated into the cryo-ET sample preparation workflow, allowing for sample optimisation before transfer to the TEM for tilt series acquisition. In this case, the 4D-STEM analysis not only allows local thickness estimation, but through its implicit diffraction measurement also provides a quality control mechanism to map regions of vitreous and crystalline ice across the lamella. We foresee a further combination with fluorescence microscopy (FM) in correlative FM modalities integrated in a FIB-SEM[36] and three-beam coincident FM-FIB-SEM instruments,[37,38] where the fluorescence microscope could also be used for in situ quality control using light-conversion 2D-STEM as we showed here, in addition to fluorescence navigation and ROI localization. In the final polishing steps, the real lamella thickness can be measured (e.g. at a local spot away from the ROI targeted for TEM analysis) and together with fluorescence-based localization microscopy produce cryo-ET samples containing the ROI in a lamella of chosen thickness.

Acknowledgements

Conflict of Interest

R.S., D.B., J.H. and A.J. are inventors on a provisional patent application for in-situ quality inspection in cryogenic focused ion beam milling (N2032641). D.B. is an employee of Delmic B.V. and J.H. has financial interest in Delmic B.V.

Author Contributions

Conceptualisation: R.S., V.K., J.H., A.J. Data curation: J.H., A.J. Formal analysis: R.S., M.S. Funding acquisition: V.K., J.H., A.J. Investigation: R.S., T.L, D.B. Methodology: R.S. Project administration: V.K., J.H., A.J. Resources: C.T.,T.L, M.S., K.M. Software: R.S. Supervision: V.K., J.H., A.J. Validation: D.B. Visualization: R.S. Writing - original draft: R.S., A.J. Writing - review & editing: D.B., M.S., K.M., V.K., J.H., A.J.

Data Availability Statement

The data that support the findings of this study are openly available in 4TU ResearchData at https://doi.org/10.4121/21365268 , reference number 21365268. The q4STEM analysis code is freely available at https://gitlab.tudelft.nl/ajlab/q4stem.

[1] R. M. Glaeser, K. H. Downing, *Ultramicroscopy* **1993**, *52*, 478.
[2] M. Marko, C. Hsieh, R. Schalek, J. Frank, C. Mannella, *Nat. Methods* **2007**, *4*, 215.
[3] H. M. E. Duyvesteyn, A. Kotecha, H. M. Ginn, C. W. Hecksel, E. V. Beale, F. de Haas, G. Evans, P. Zhang, W. Chiu, D. I. Stuart, *Proc. Natl. Acad. Sci.* **2018**, *115*, 9569.
[4] F. R. Wagner, R. Watanabe, R. Schampers, D. Singh, H. Persoon, M. Schaffer, P. Fruhstorfer, J. Plitzko, E. Villa, *Nat. Protoc.* **2020**, *15*, 2041.
[5] M. W. Martynowycz, M. T. B. Clabbers, J. Unge, J. Hattne, T. Gonen, *Proc. Natl. Acad. Sci.* **2021**, *118*, 1.
[6] F. I. Allen, N. R. Velez, R. C. Thayer, N. H. Patel, M. A. Jones, G. F. Meyers, A. M. Minor, *Nanoscale* **2019**, *11*, 1403.
[7] D. Mullick, K. Rechav, L. Leiserowitz, N. Regev-Rudzki, R. Dzikowski, M. Elbaum, *Faraday Discuss.* **2022**, *240*, 127.
[8] W. van Mierlo, D. Geiger, A. Robins, M. Stumpf, M. L. Ray, P. Fischione, U. Kaiser, *Ultramicroscopy* **2014**, *147*, 149.
[9] C. Lang, M. Hiscock, C. Dawson, C. Hartfield, *Microelectronics Reliability* **2014**, *54*, 1790.
[10] A. Rigort, F. J. B. Bäuerlein, E. Villa, M. Eibauer, T. Laugks, W. Baumeister, J. M. Plitzko, *Proc. Natl. Acad. Sci.* **2012**, *109*, 4449.
[11] W. J. Rice, A. Cheng, A. J. Noble, E. T. Eng, L. Y. Kim, B. Carragher, C. S. Potter, *J. Struct. Biol.* **2018**, *204*, 38.
[12] A. P. Conlan, E. Tillotson, A. Rakowski, D. Cooper, S. J. Haigh, *J. Microsc.* **2020**, *279*, 168.
[13] T. Volkenandt, E. Müller, D. Gerthsen, *Microsc. Microanal.* **2014**, *20*, 111.
[14] R. Skoupy, J. Nebesarova, M. Slouf, V. Krzyzanek, *Ultramicroscopy* **2019**, *202*, 44.
[15] H. Kim, T. Negishi, M. Kudo, H. Takei, K. Yasuda, *J. Electron Microsc.* **2010**, *59*, 379.
[16] M. Dapor, N. Bazzanella, L. Toniutti, A. Miotello, S. Gialanella, *Nucl Instrum Methods Phys Res B NUCL INSTRUM METH B* **2011**, *269*, 1672.
[17] M. Dapor, N. Bazzanella, L. Toniutti, A. Miotello, M. Crivellari, S. Gialanella, *Surf. Interface Anal.* **2013**, *45*, 677.
[18] T. Volkenandt, E. Müller, D. Z. Hu, D. M. Schaadt, D. Gerthsen, *Microsc. Microanal.* **2010**, *16*, 604.
[19] A. Garitagoitia Cid, R. Rosenkranz, M. Löffler, A. Clausner, Y. Standke, E. Zschech, *Ultramicroscopy* **2018**, *195*, 47.
[20] M. Pfaff, E. Müller, M. F. G. Klein, A. Colsmann, U. Lemmer, V. Krzyzanek, R. Reichelt, D. Gerthsen, *Journal of Microscopy* **2011**, *243*, 31.
[21] R. Skoupy, T. Fort, V. Krzyzanek, *Nanomaterials* **2020**, *10*, 332.
[22] C. Ophus, *Microsc. Microanal.* **2019**, *25*, 563.
[23] B. H. Savitzky, S. E. Zeltmann, L. A. Hughes, H. G. Brown, S. Zhao, P. M. Pelz, T. C. Pekin, E. S. Barnard, J. Donohue, L. Rangel DaCosta, E. Kennedy, Y. Xie, M. T. Janish, M. M. Schneider, P. Herring, C. Gopal, A. Anapolsky, R. Dhall, K. C. Bustillo, P. Ercius, M. C. Scott, J. Ciston, A. M. Minor, C. Ophus, *Microsc. Microanal.* **2021**, *27*, 712.

[24] K. C. Bustillo, S. E. Zeltmann, M. Chen, J. Donohue, J. Ciston, C. Ophus, A. M. Minor, *Acc. Chem. Res.* **2021**, *54*, 2543.

[25] R. Skoupy, V. Krzyzanek, *Microsc. Microanal.* **2021**, *27*, 1602.

[26] R. Skoupy, D. B. Boltje, J. P. Hoogenboom, A. J. Jakobi, *Microsc. Microanal.* **2022**, *28*, 1210.

[27] M. Slouf, R. Skoupy, E. Pavlova, V. Krzyzanek, *Nanomaterials* **2021**, *11*, 962.

[28] V. Krzyzanek, R. Reichelt, *Microsc. Microanal.* **2003**, *9*, 110.

[29] W. Kraus, G. Nolze, *J. Appl. Crystallogr.* **1996**, *29*, 301.

[30] S. Gražulis, D. Chateigner, R. T. Downs, A. F. T. Yokochi, M. Quirós, L. Lutterotti, E. Manakova, J. Butkus, P. Moeck, A. Le Bail, *J. Appl. Crystallogr.* **2009**, *42*, 726.

[31] R. Skoupy, STEMDIFF - powder electron diffraction in SEM, **2022**, https://mathworks.com/matlabcentral/fileexchange/99819-stemdiff-powder-electron-diffraction-in-sem, (accessed: December 2022).

[32] W. Zuidema, P. Kruit, *Ultramicroscopy* **2020**, *218*, 113055.

[33] FAST-EM: automated multibeam electron microscope, https://www.delmic.com/en/products/fast-imaging-solutions, (accessed: December 2022).

[34] P. Schweizer, P. Denninger, C. Dolle, E. Spiecker, *Ultramicroscopy* **2020**, *213*, 112956.

[35] M. Slouf, R. Skoupy, E. Pavlova, V. Krzyzanek, *Materials* **2021**, *14*, 7550.

[36] S. Gorelick, G. Buckley, G. Gervinskas, T. K. Johnson, A. Handley, M. P. Caggiano, J. C. Whisstock, R. Pocock, A. de Marco, *eLife* **2019**, *8*, e45919.

[37] D. B. Boltje, J. P. Hoogenboom, A. J. Jakobi, G. J. Jensen, C. T. Jonker, M. J. Kaag, A. J. Koster, M. G. Last, C. de Agrela Pinto, J. M. Plitzko, S. Raunser, S. Tacke, Z. Wang, E. B. van der Wee, R. Wepf, S. den Hoedt, *eLife* **2022**, *11*, 1.

[38] S. Li, Z. Wang, X. Jia, T. Niu, J. Zhang, G. Yin, X. Zhang, Y. Zhu, G. Ji, F. Sun, *Nat. Methods* **2023**, *20*, 276.